3D Seismic Endoscopy: Multiscale analysis and Dynamic azimuthal filtering of borehole waves

Henri-Pierre Valero, Ginette Saracco

Geophys. J. Int. (2005) **161,** 813–828 doi: 10.1111/j.1365-246X.2005.02616.x

3-D seismic endoscopy: multiscale analysis and dynamic azimuthal filtering of borehole waves

Henri Pierre Valero[1,*] and Ginette Saracco[2,†]

[1]*IPGP & CNRS-UMR*-6118, *Géosciences-Rennes, Campus de Beaulieu, Rennes, France*
[2]*CNRS-UMR*-6118, *Géosciences Rennes, Campus de Beaulieu, Rennes, France*

Accepted 2005 February 11. Received 2004 December 1; in original form 2004 January 26

SUMMARY

We previously proposed a method of seismic endoscopy and a related prototype tool to acquire directional information and to produce three-dimensional (3-D) seismic images in a cylindrical volume surrounding a borehole, with an investigation radius of several metres. Basic imaging algorithms were developed where the azimuthal move out (AMO) process is combined to a timescale method to refocus directional information and analyse the surrounding medium. Further processing tools, however, were necessary for separating the various types of waves recorded. The present paper describes a multiscale and dynamic azimuthal filtering to separate the far-field waves from borehole or tube waves, generated by the pipe. We call this filter Stoneley move out (SMO), because it characterizes Stoneley waves associated with the tube. It is then possible to reconstruct details of the far field by an inverse wavelet transform. The comparison with classical methods such as the covariance method is discussed. Applications on noisy synthetic and experimental data are presented.

Key words: azimuthal move out, complex continuous wavelet transform, demodulation, dynamic Stoneley move out, multiscale filtering, three-dimensional geophysical imaging.

1 INTRODUCTION

The main objective in borehole imaging is to obtain an accurate three-dimensional (3-D) seismic image to safely operate in a cylindrical volume surrounding the well. Such information is of interest for geotechnical studies in tunnel monitoring, rock stratigraphy, water resource evaluation (Kelly & Mares 1993; Nobes 1996), chemical or nuclear waste disposals (Hardin *et al.* 1987; Burger 1992) and in reservoir engineering (Avis & Annan 1989). The knowledge of a fracture position and its thickness is important for the reorganization of a reservoir monitoring, tunnel construction, or for the localization of a nuclear waste storage. Most borehole geophysical techniques cannot do azimuthal acquisition along the vertical axis (the depth z), which is important for decisions in sensitive cases such as nuclear waste disposal (Hardage 1983; Oristaglio 1985; Hornby 1989; Paillet & Cheng 1991). Therefore, a 3-D analysis including textural and structural information of the formation surrounding the well in a given azimuth, is a challenge.

*Now at: Schlumberger Doll Research, 36 Old Quarry Road, Ridgefield, CT 06810, USA. E-mail: hvalero@ridgefield.oilfield.slb.com
†Now at: CNRS-UMR 6635, CEREGE, Département de Géophysique, Europôle de l'Arbois, BP 80, F-13545 Aix-en-Provence, France. E-mail: ginet@cerege.fr

The 3 classical degrees of freedom that sonic or vertical seismic profile (VSP) tools possess are the offset ζ, the depth z of the receiver and the time t of the recorded signal. The main objective of the sonic tool is to determine from an array of acoustic data, the slowness of the formation (Kimball & Marzetta 1987; Paillet & Cheng 1991), whereas the main interest of the VSP tool is to calibrate the surface seismic and in some cases to characterize the structure around the borehole (Hornby 1989). If the sonic tool is not able to perform directional acquisition, multicomponent VSP acquisitions, where azimuthal information is provided in an indirect way, cannot detect small discontinuities as a result of the frequency range of the source (80–100 Hz). The only tool providing azimuthal measurements is the so-called televiewer, which is composed of directional transducers (Zemanek *et al.* 1970). However, it does not allow a deep penetration in the formation because of the very high frequencies of transducers (500 MHz). This renders impossible the imaging of the formation surrounding the well. Some others techniques like Georadar (Fisher 1992) were tested but have limited use for reservoir engineering owing to the frequent presence of shale layers at the top of reservoirs.

In this context, some studies concerning the design of a specific tool (Fig. 1) and a method called seismic endoscopy (Valero 1997; Valero *et al.* 2001) have been conducted to produce a 3-D azimuthal seismic image in a cylindrical volume with an investigation radius of several metres. The introduction of the directional azimuthal

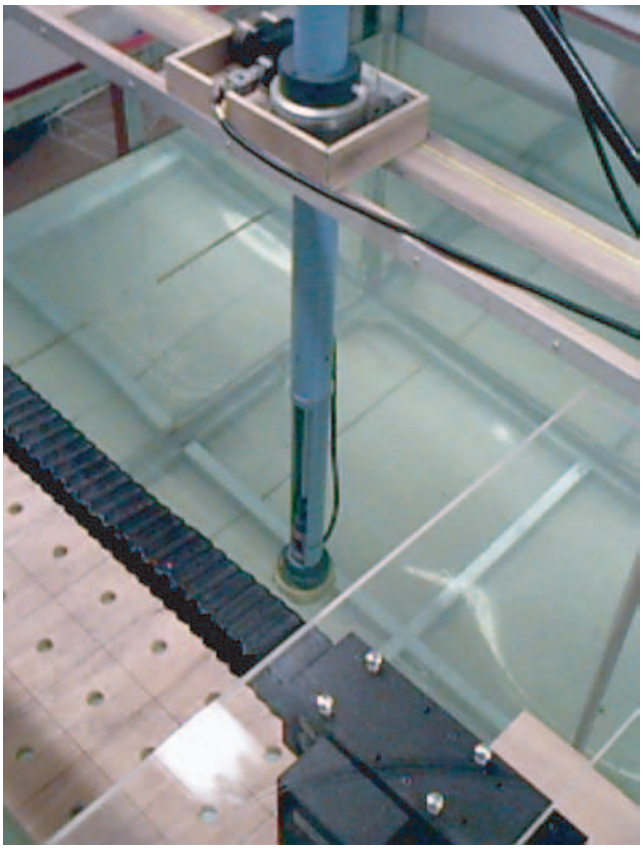

Figure 1. Directional probe during an experiment in the water tank. The isotropic source is located vertically at the bottom of the probe. Above is the window of absorbing material, where the receiver cell is included. The cell composed of two directional receivers is of variable offset (distance source–receivers is between 15 and 80 cm). The stepping motor located at the top of the probe controls its rotation in the horizontal plane.

parameter θ implied an additional degree of freedom with specific processing that a sonic or VSP tool does not possess. Fig. 1 presents the prototype probe during an experiment in the acoustic tank. This probe makes it possible to obtain directional azimuthal measurements in the horizontal and vertical planes around the borehole, owing to the rotation and translation of the tool in the well. This prototype was developed to operate in a frequency range of 20–200 kHz with an omnidirectional source (hydrophone) and a directional receiver cell composed of two hydrophone receivers, vertically set above the source. Azimuthal information is obtained by rotation of the tool in the borehole while the directional acquisition and the spatial resolution are obtained from the aperture of the receiver cell and from the wavelength of the source signal. The directivity patterns of the cell (ear cell) were defined for the frequency range of the source (20–100 kHz) in both the horizontal and vertical plane. The directivity is sharp and presents a full-width half-maximum aperture of approximatley 40° (horizontal axis) and 60° (vertical axis). This is a compromise between good precision in the detection of microfractures and the possibility to hear the signal coming far from strong heterogeneities in both axes. The probe can move vertically along the well and scans the rock with an offset variation between the source and the directional receiver cell of 15–80 cm and a azimuthal sampling step of 5° (see Fig. 2). For more details on the prototype design, operating constraints and basic processing, the reader should refer to Valero (1997) and Valero *et al.* (2001).

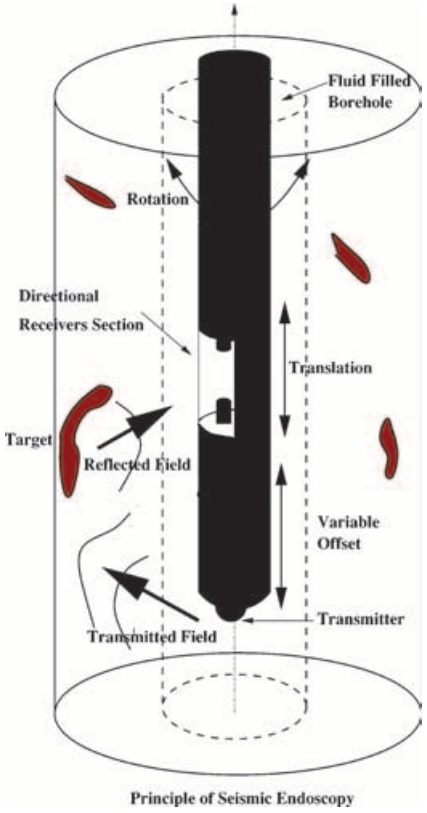

Figure 2. This figure presents the principle of seismic endoscopy. Thanks to directional receivers of the probe, we record azimuthal acquisition. By rotation and translation of the probe into the well, we acquire a cylinder volume of data.

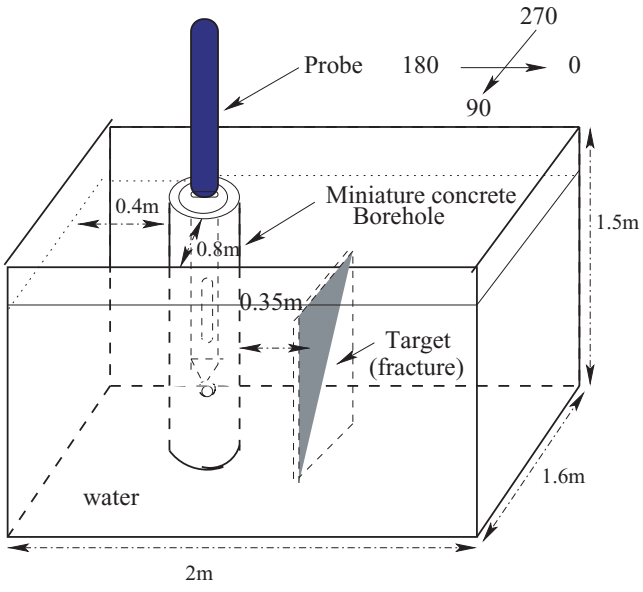

Figure 3. Principle of the experiment. The probe is put in a miniature concrete borehole. A target (metallic plate) is located outside the well at a distance of 0.35 m.

Because this concept was new, a specific processing algorithm called azimuthal move out (AMO; Valero 1997) combined with a timescale or complex wavelet method (Saracco 1994) was initially developed. This AMO processing allows us to refocus the

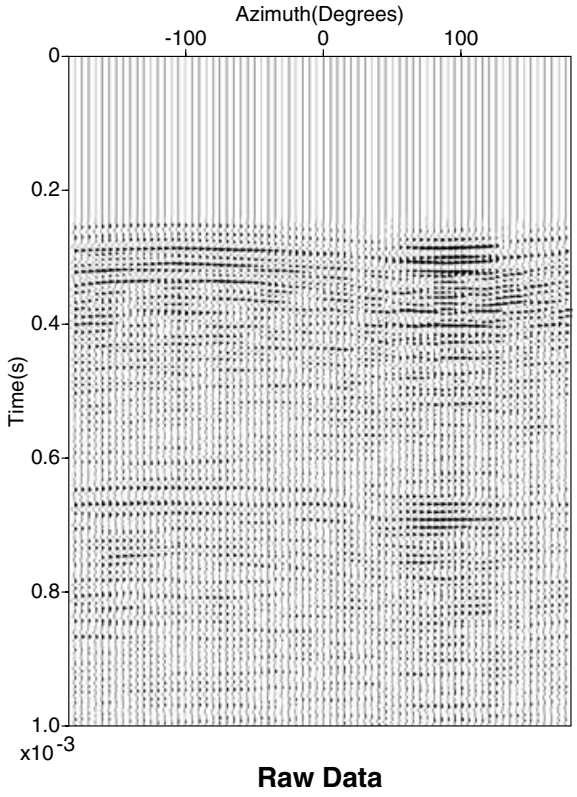

Figure 4. Experimental data recorded with the prototype probe set in the miniature concrete borehole. We note that it is impossible to detect the acoustic signature of the metallic plate, which is masked by the strong borehole waves. Remark the directive character of the probe allows us to detect a discontinuity in the concrete pipe at the azimuth of 90°.

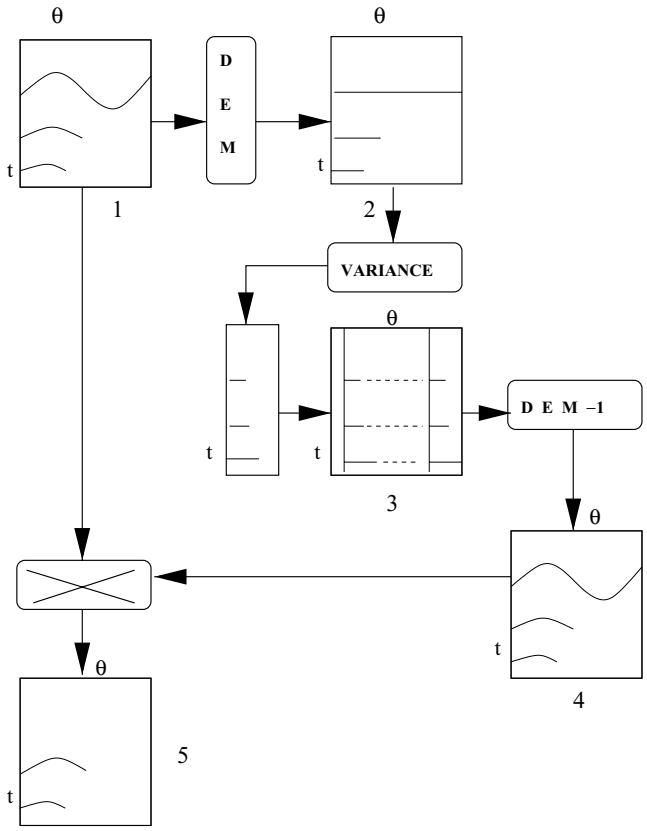

Figure 5. Process to dynamically filter the borehole waves. We start first with data recorded in the azimuth–time domain (1). The DEM correction is applied in (2). We compute the variance indicator and create a section of variance filter (3). The inverse correction (DEM^{-1}) is then applied tis filter section to recreate oscillations (4). Result of the variance filter multiplied by the input data producing the dynamic Stoneley move out (SMO) filtering of borehole waves (5).

energy of the recorded signal in the azimuthal–time domain, while the complex continuous wavelet transform (CCWT) allows us to select the signal of interest among the various borehole waves. These preliminary processes were successfully tested on experimental data in an acoustic laboratory (Valero *et al.* 2001). When the recorded signal needs to be deconvolved from the instrumental devices and/or the source effect, the methodology developed in Saracco & Tchamitchian (1990) and Valero *et al.* (2002) is applied. This study encountered the well-known problem of imaging around the well, because of the large amplitude difference between the borehole waves and the far-field reflected waves, of interest. Note that, in this study, borehole waves are the waves related to the borehole shapes, as opposed to the far-field reflected waves coming from the medium surrounding the well. These preliminary experiments show that the key part of borehole imaging is to separate small energy of far-field events from strong energy of borehole waves. Therefore, we concentrated efforts to develop filtering methods that can discriminate between the signal of interest, the noise and the high amplitude of borehole waves. If the AMO correction provided good results in academic configurations (Valero *et al.* 2001), a dynamic and multiscale filtering (MSF) is necessary in real-life situations to discriminate among contributions of the various waves and to detect and localize fractures in complex media.

This paper focuses on dynamic and MSF of borehole waves, independently of the location of the probe in the well and of the amplitude ratio of the far-field reflected waves. Its aim is to propose an accurate 3-D seismic imaging. The azimuthal information θ carried by the specific tool is added to the cylindrical volume data (ζ, z, t).

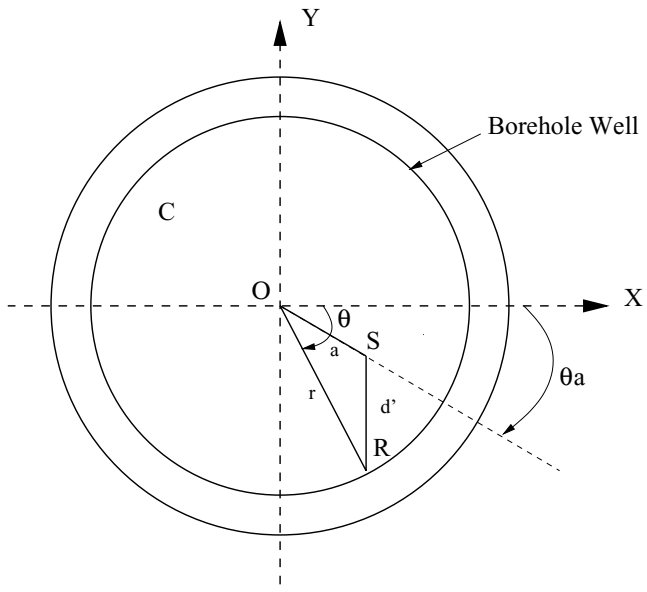

Figure 6. Principle of the demodulation (DEM) correction. When the tool is off-centred (*S* position) it induces a sinusoidal shape on the recorded data. The tool is located in *O* if it is well centred in the hole.

In Section 2, we present the experimental set-up developed to validate our processing algorithm in the acoustic tank. The prototype tool is set in a miniature concrete pipe with a scatterer located outside the well. Moreover, the concrete pipe presents some defective responses in the same frequency range of the scatterer and borehole waves, as it occurs in field experiments. The dynamic azimuthal correction called Stoneley move out (SMO) is presented Section 3, first on noisy synthetic data, then on acoustic experimental data. SMO allows us to focus the energy of borehole waves according to the off-centring of the tool, with a dynamic filtering in the azimuthal–time domain. This filtering will be shown to have some limitations, particularly if the noise and the signal of interest are in the same frequency range. To avoid such limitations, we developed, in Section 4, a multiscale decomposition of the total reflected field. Some characteristics of the filtered far field can be then reconstructed. This reconstruction is based on the direct and inverse continuous wavelet transform using the properties of the reproducing kernel of the transform (Saracco 1989). The proposed method is applied efficiently, first to synthetic complex waves trains in the presence and absence of noise, then to real experimental data recorded in the acoustic tank. Results of reconstruction imaging from the dynamic MSF are compared, in Section 5, to the well-known singular value decomposition (SVD), generally used to filter borehole waves (Hsu 1990). Conclusions and perspectives are given in Section 6.

2 LABORATORY ACOUSTIC EXPERIMENT

A miniature cement pipe, used in civil engineering is introduced vertically in the water tank to obtain strong tube waves like in real field experiments (Tubman *et al.* 1984; Winkler *et al.* 1989). The probe is set inside this concrete pipe and a metallic plate is located outside at a distance $d = 0.35$ m and at the azimuth 0° from the probe. Fig. 3 presents the design of the experiment. The source signal, selected by the user via a numerical generator, is amplified before to be sent to the hydrophone source of the probe. The reflected pressure field measured by the directive receiver cell (or ear) is then pre-amplified before to be sampled synchronously ($fe = 500$ kHz) by the analogue-to-digital (A/D) converter. The azimuthal rotation of the tool is controlled by a device allowing an angular precision of 0.1°. For each experiment, 72 traces of 2048 time samples per common offset are measured (the increment is 5°). All experiments are automatized and controlled by the computer. One complete acquisition ($0 < \theta < 360°$) takes less than 2 min. The source signal used in these experiments is a Ricker function in time (second derivative of a Gaussian function) defined as

$$r(t) = \left[1 - 2(\pi f_c t)^2\right] \exp\left[-(\pi f_c t)^2\right], \quad (1)$$

where f_c is the central frequency of the hydrophone source ($f_c = 50$ kHz).

The metallic plate in this experiment mimics a discontinuity of a medium, or a fracture. It is not identical to real conditions because of the presence of water around the pipe rather than a solid medium. The use of water for the surrounding medium is interesting for testing our algorithms. The penetration of the signal into the formation depends on the frequency range of the source: the lower the frequency, the deeper the distance of investigation. Besides, the properties of the surrounding medium do not play an important role in the directivity properties of the tool (Valero *et al.* 2001), but in the penetrating power of the source signal as a result of scattering, diffusion, attenuation and/or absorption. A fracture, microcavity appears as a discontinuity in the acoustic velocity and pressure fields, and creates a reflected/diffracted wavefield. Our objective is to filter out the borehole waves in order to recover a weak reflected/diffracted wavefield caused by a microcavity or interface and that could be blurred by the strong borehole waves.

Fig. 4 presents the experimental raw data. The strong reflection measured around the azimuth $\theta = 90°$ corresponds to a longitudinal junction in the concrete pipe. This information demonstrates the efficiency of our directional probe. As we can observe, the detection of the signature of the metallic plate is masked by strong borehole waves generated in the same spectral range as the reflected/diffracted signal. We also see that the recorded data show a similar level of complexity as a real record, which allows us to validate our algorithms on a realistic data set.

3 DYNAMIC AZIMUTHAL FILTERING OF BOREHOLE WAVES

3.1 Principle of the method

The SMO processing is a dynamic filtering of specific waves generated in the borehole (for example Stoneley or tube waves) that mask the information coming from the surrounding medium. The principle is based on the arrival time of borehole waves in the

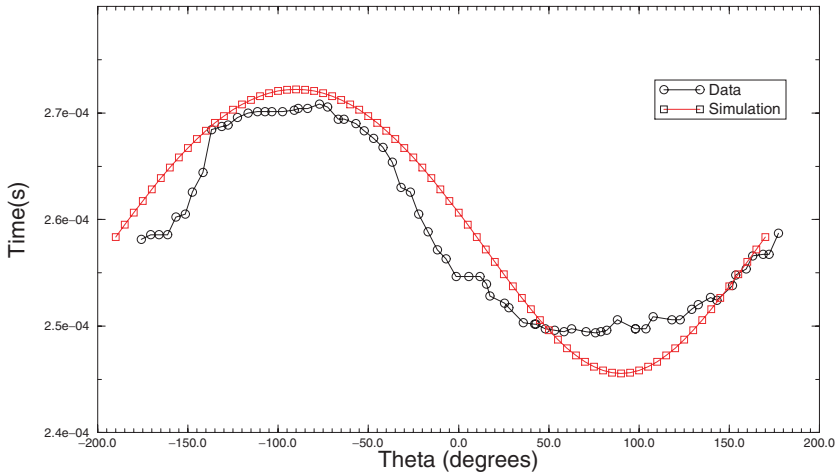

Figure 7. Comparison between simulation and data obtained by automatic time picking. Note the good agreement between simulated and real data.

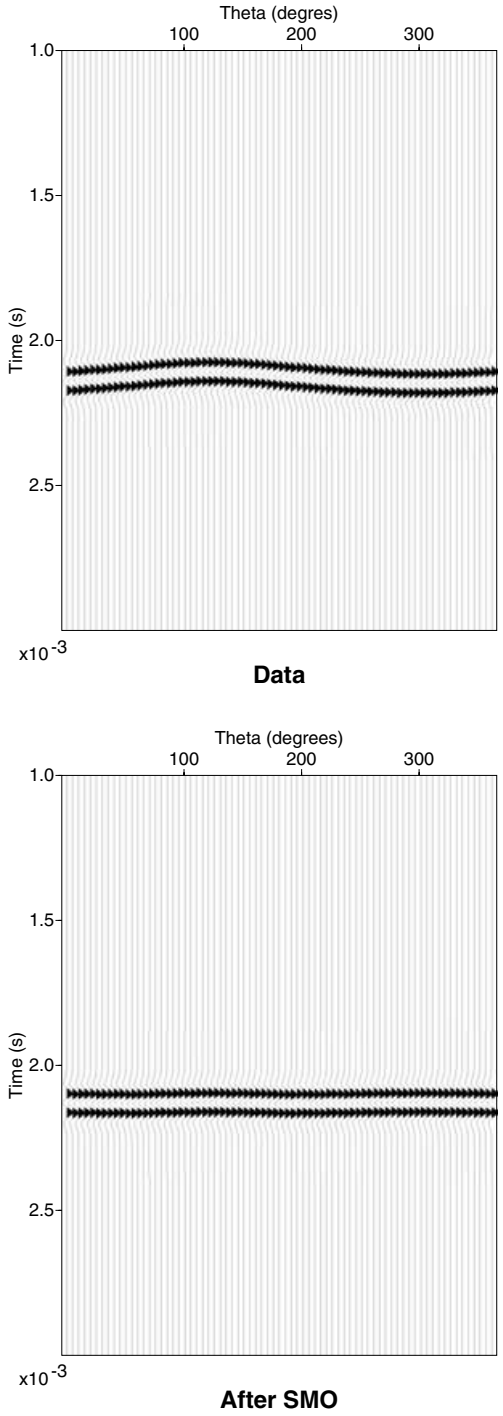

Figure 8. Demodulation (DEM) correction for two borehole waves propagating in the hole. After correction, both arrivals are flattened, as expected.

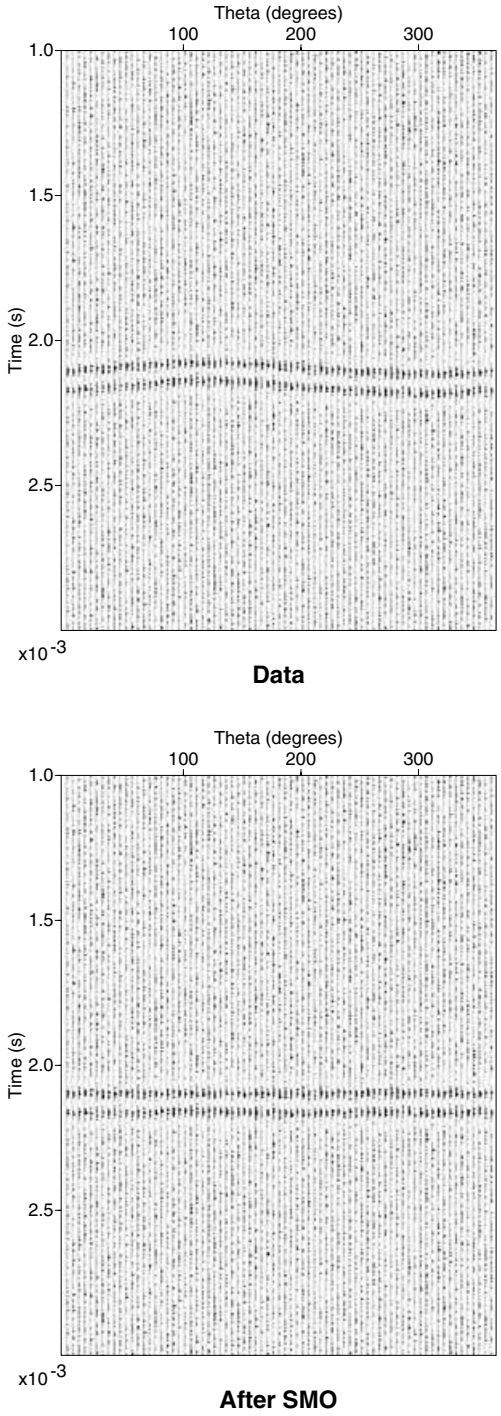

Figure 9. Demodulation (DEM) correction in presence of noise. Even if the noise level is high, the DEM algorithm is able to flatten the two arrivals. This result proves the robustness of this process.

(t, z, ζ) domain and their invariance property versus azimuth in the (θ, t) plane. Since the tool is centred in the pipe, the wave front of borehole waves will be represented as a continuous line in the (θ, t) plane. The higher the off-centring of the tool, the greater the modulation of the arrival time of the borehole waves. This SMO filtering involves two steps: first the parameters of eccentricity are computed to correct the data from the sinusoidal shape as a result of the off-centring of the probe. We called this operation demodulation (DEM). An inverse demodulation (DEM^{-1}) is also defined and used to verify our processing. Secondly, the calculation in the azimuthal domain of the variance of the wave front duration allows us to filter automatically borehole waves. The dynamic SMO filter is the result of two operations: a demodulation and an azimuthal stacking. To validate this method, we applied it to both on synthetic and acoustic experimental data. Fig. 5 presents the whole processing sequence. The details of the method will be now presented.

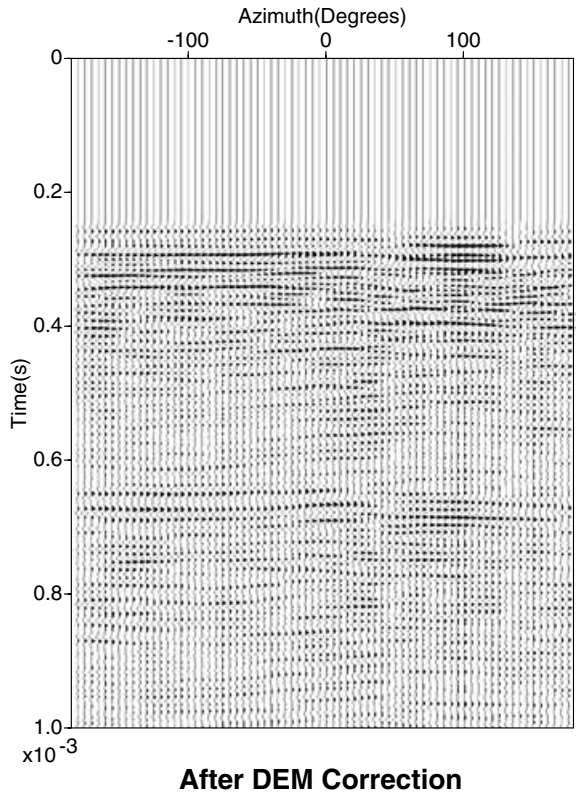

Figure 10. Raw data after the demodulation (DEM) correction. Note how the main oscillation was flattened as expected.

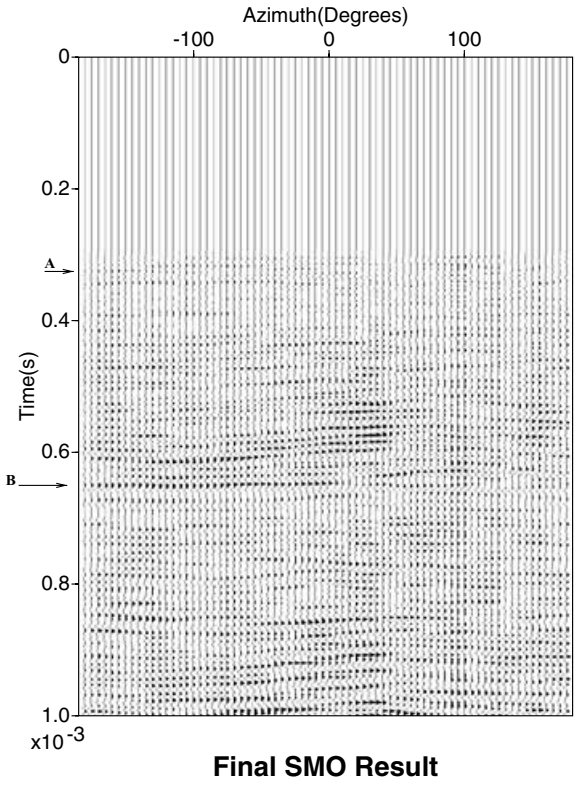

Figure 11. Result obtained after the dynamic Stoneley move out (SMO) filtering on raw data. Most of borehole waves have been filtered. It is now possible to detect the acoustic signature of the metallic plate around $\theta < 0^\circ$. We also see some reflections as a result of the junction effect of the pipe (A) and of the bottom of the tank (B).

Consider a tool located in a borehole of radius r containing a fluid (mud) of sound velocity $c_{\rm m}$. Fig. 6 describes the geometry of the problem for a fixed depth z, in the section $(t, z = Cst, \zeta, \theta)$. The position of the tool can be defined by the eccentricity a (distance between the centre O of the pipe and the position S of the probe in the pipe) and θ_a (the angular position associated to the eccentricity a). r denotes the distance between the pipe and the probe in the direction θ. Using these notations, we can express the zero offset reflected traveltime of borehole waves, in the θ, r plane assuming a high-frequency asymptotic condition:

$$t(\theta) = \sqrt{t_o^2 + t_a^2 - 2t_o t_a \cos[\theta - \theta_a]}, \tag{2}$$

where $t_o = \frac{r}{c_{\rm m}}$ and $t_{\rm a} = \frac{a}{c_{\rm m}}$.

This is the DEM equation. The assumption is tested by picking up iteratively the arrival times on the data recorded during the experiment and compared with the simulated values calculated from eq. (2). Although the DEM equation was obtained under a high-frequency assumption, it can be seen (Fig. 7) that the predicted arrival times are in good accordance (phase and amplitude) with experimental data. We note that eq. (2) used to perform a dynamic correction of the bias in the arrival times presents some similarities with the normal move out (NMO) equation (Dobrin 1983; Burger 1992).

The estimation of the two parameters of eccentricity a and $\theta_{\rm a}$ is obtained for a given angle θ and time t_o by an iterative local optimization of the least-squares misfit function between the recorded time and the computed arrival time from eq. (2):

$$\sum_{i=1}^{N} \left[t_{\rm obs} - t_{\rm calc}(a, \theta_a)\right]^2. \tag{3}$$

The construction of the SMO filtering is then based on the identification of plane reflectors (continuous flat line versus azimuth) in the (θ, t) domain (step 2, Fig. 5). To detect such events, the variance along curves whose arrival times are $t(\delta\theta)$ for both given θ and t_o can be computed in the azimuthal domain as follows:

$$\mathrm{Var}(t) = \frac{1}{N} \sum_{i=1}^{N} \left[p^2(\theta_i, t) - \overline{p}^2(\theta_i, t)\right], \tag{4}$$

where $p(\theta_i, t)$ represents a trace and $\overline{p}$ is the average at the time t along the azimuth θ. N is the number of traces; in our specific case it is equal to 72. This stacking increases the signal-to-noise ratio and cancels all echoes coming from the far field that do not possess azimuthal invariance. When Var(t) is small it means that the event at the time t is continuous versus azimuth and corresponds to borehole waves. Echoes coming from borehole shape are enhanced and present a flat line in the azimuthal–time domain, as expected.

A filter section is automatically built from the N traces of variance Var(t) and corrected by the DEM^{-1} process. This dynamic SMO filtering is then applied to rough data (see Fig. 5). Borehole waves multiplied by small variance values are cancelled while the far-field waves are emphasized by high variance values. The amplitude level of the waves coming from the formation around the borehole is automatically increased.

3.2 Application to synthetic data

We first applied this method to synthetic data free of noise. The geometrical parameters of the off-centring of the tool were chosen

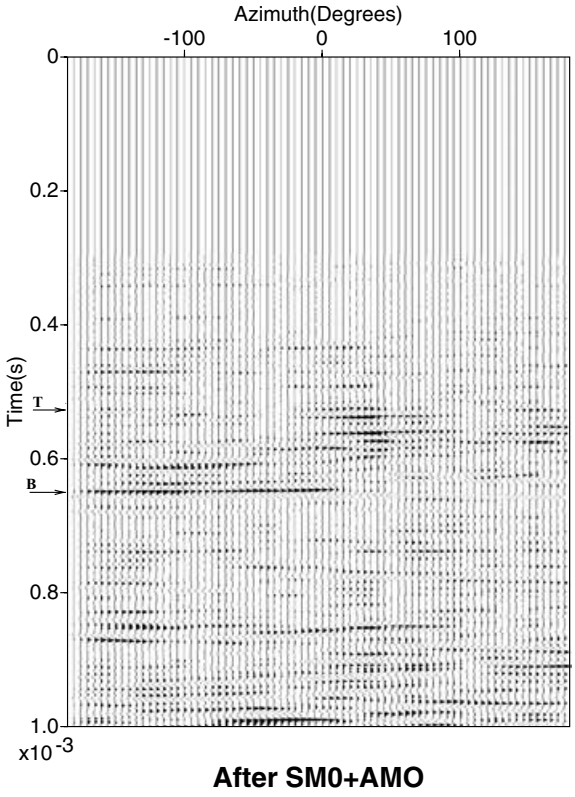

Figure 12. Final result after the Stoneley move out (SMO) and the azimuthal move out (AMO) correction. The energy is refocused in the azimuth–time domain thanks to the AMO correction. The final section shows clearly the echo corresponding to the target (T) we wanted to detect.

according to real experimental parameters with an eccentricity $a = 0.03$ m and a deviation $\theta_a = 120^\circ$, for a borehole diameter r of 0.12 m. The first group of tests consists of computing the wave front arrival time of two borehole waves using ray theory without noise. The sound velocity in the borehole is set at 1486 m s^{-1} for our simulations (sound velocity for a temperature of water of 20.2 °C). Fig. 8 presents the results before and after the DEM correction. As expected, the DEM corrects successfully the data from the off-centring of the tool and flattens the observed sinusoid shape. A second series of tests using the same set of data was considered in the presence of a white Gaussian noise with a signal-to-noise ratio $sn = 2$:

$$\hat{s}(t) = s(t) + \text{scale} \times \text{noise},$$

with

$$\text{scale} = \left(\frac{1}{sn}\right) \times \left[\frac{|\max(\text{signal})|}{\sqrt{2N}}\right].$$

Fig. 9 presents the results in the presence of noise. Even in the presence of a high level of noise, the algorithm corrects the data from the off-centring of the tool. This test shows the robustness and the efficiency of the dynamic DEM correction.

3.3 Application to acoustic experimental data

The complete processing of experimental data is shown Fig. 4. Fig. 10 shows the result after the DEM correction of rough data. The eccentricity parameters found are respectively $a = 0.01$ m and $\theta_a = -115^\circ$. As expected, the first arrival is flattened. The final result is presented Fig. 11, where the two-dimensional (2-D) variance filter is applied to cancel or at least to minimize the effect of the borehole waves. Most of borehole waves have been removed, improving the signal-to-noise ratio. It is now possible to observe in Fig. 11 the acoustic signature of the metallic plate located at the azimuth $\theta = 0^\circ$ around the time 0.5 ms $< t <$ 0.6 ms, together with a signal of weak energy at the azimuth $\theta = 90^\circ$ as a result of the junction effect of the pipe (Fig. 11, arrow A). Nevertheless, a first and strong arrival wave front of the direct reflected waves (specular echo) generated by the bottom of the water tank is still present (Fig. 11, arrow B). This direct wave is partially filtered by our processing around the defect.

Finally, an AMO correction is applied to refocus the energy spread out in the azimuthal–time domain. The main characteristic of the AMO processing is to sharpen the angular resolution of the probe by correcting the transfer function of the receivers. The reader can refer to Valero *et al.* (2001) for details regarding this processing. Fig. 12 presents the result of this correction. The acoustic signature of the metallic plate is located around the time $t = 0.54$ ms (arrow A), for $0^\circ < \theta < 40^\circ$ centred on $\theta = 20^\circ$ with some multiple reflections inside the object. This azimuthal difference in the localization of the metallique plate is the result of a weak rotation of the receiver cell of the prototype probe after several experiments, compared with its original position. A strong wave front located at the time $t = 0.64$ ms can be observed (Fig.12, arrow B) . This second reflector partially hidden by the metallic plate and enhanced by the AMO correction corresponds to a part of the field reflected by the bottom of the tank. Nevertheless, it is now possible to locate the position of the object. The remaining arrivals do not introduce difficulties in the detection of the metallic plate position. The comparison of this final result with the raw data set demonstrates clearly the efficiency and the robustness of this SMO filtering.

4 MULTISCALE FILTERING

4.1 Recall: continuous wavelet transform

The continuous wavelet transform is a well-known method developed by Alex Grossmann and Jean Morlet (Grossmann & Morlet 1984). Its first applications were in quantum mechanics, geophysics and acoustics. Its efficiency was demonstrated in various domains and different objects as fractal functions, musical synthesis, turbulence and wave propagation (Morlet *et al.* 1982; Saracco 1989). The properties of the CCWT (isometry, linearity, scaling and covariance) and of the analysing wavelet itself (regularity and progressivity) that we can add, allow us to study independently the various contributions constituting the reflected or the transmitted field and to obtain methods for numerical computation of the potential field. The wavelet transform of the Green's function is more regular than the Green's function itself. This regularizing property allows precise localization of various wave fronts and selective reconstruction of the acoustic or seismic pressure field (Saracco 1994).

This transformation allows to decompose an arbitrary time or space dependence signal $s(p)$ into elementary contributions of functions called wavelets obtained by dilation and translation of a mother or analysing wavelet $g(p)$. Let p be the time variable in our data. We can do a local and accurate analysis (at $\triangle f/f = C^{st}$) in the time–frequency or timescale half-plane (b, a) (Grossmann *et al.* 1989). The wavelet coefficients at a point (b, a) are defined

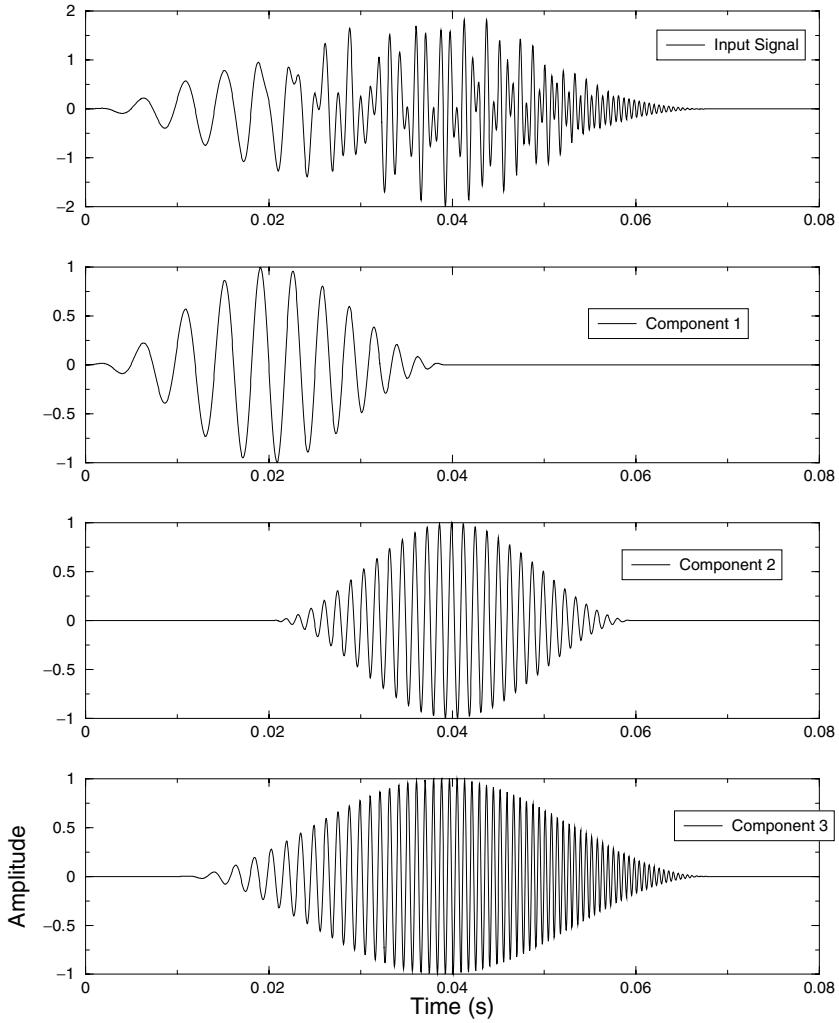

Figure 13. Presentation of input signal used in this study. The top curve is the signal of interest built by summation of the different components presented below.

by the scalar product of the signal $s(t)$ with the wavelets family $\frac{1}{\sqrt{a}}g(\frac{t-b}{a})$:

$$S(b,a) = a^{-1/2}\int s(t)\overline{g}\left(\frac{t-b}{a}\right)dt. \tag{5}$$

If g is a complex analysing wavelet, $\overline{g}$ is the complex conjugate of g, dilated in time of a ($a > 0$) and translated in time of b ($b \in \mathcal{R}$). a and b are respectively the scale (or dilation) parameter and the translation parameter (see Appendix for more details and demonstrations).

In order to correctly define and give a physical meaning to the phase of the wavelet coefficients, the analysing wavelet must verify the analytic or progressive property [i.e. $\hat{g}(\omega) = 0, \omega < 0$]. The calculation of the wave fronts of different wave contributions (Saracco 1994) and their spectral components can be performed precisely without artefacts or interferences as a result of no Fourier components on the negative axis.

4.2 Principle of the multiscale filtering (MSF)

Let consider a signal $s(t)$ composed by the sum of m waves f_i of various spectral contents and/or arrival times. We assume that these waves are not isolated but present some weak interferences. If we compute the wavelet transform of this signal we obtain, thanks to the linearity property of the transform, a spread of its energy in the time–frequency space:

$$S_s(b,a) = \sum_{i=1}^{m} S_{f_i}(b,a). \tag{6}$$

In order to extract a component $f_i(t)$ from the total wavelet coefficient S_s, we have to define a mask $M_{fi}(b,a)$ in the half-plane (b,a) and use, under some conditions, the reconstruction formula of the CCWT on the pattern of interest. In experimental situations, noise is generally present; it is therefore necessary to construct a mask, to define a threshold based on the maximum of energy contained in the time–frequency space.

The principle of the wavelet filtering consists of extracting, from the timescale half-plane, the signal $f_i(t)$ from $S_s(t)$ by using the reproducing equation (Appendix eq. A9) and the properties of the reproducing kernel and the continuous wavelet transform [$S_{fi}(b,a)$; Saracco 1989]. The mask is defined with respect to a threshold χ, according to the total energy and the signal-to-noise ratio. Each mask allows us to define a polygon function h associated with each

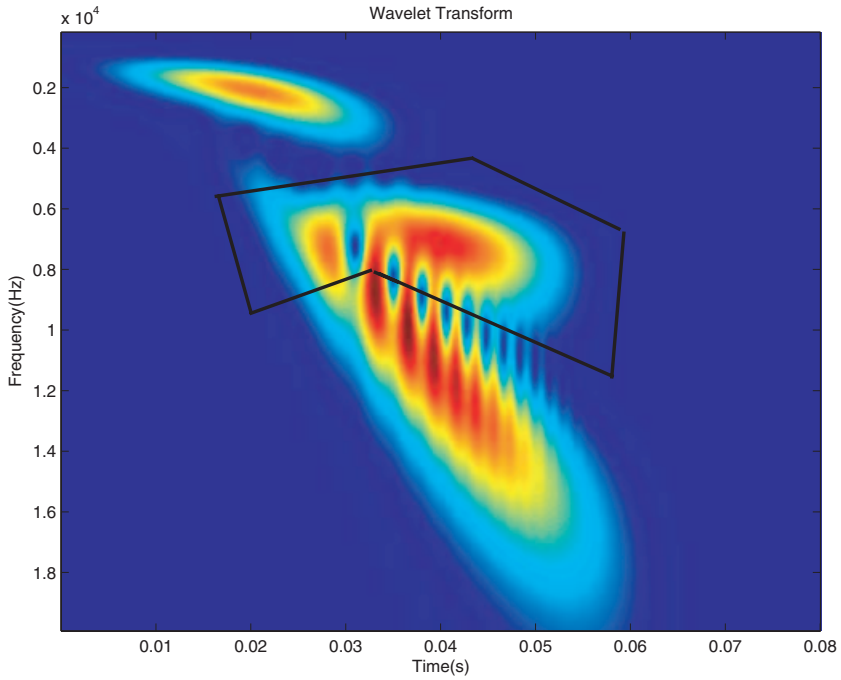

Figure 14. Modulus of the complex continuous wavelet transform (CCWT) of the studied signal. We clearly observe the different components that comprised the signal of interest. The black polygon corresponds to the truncature of the wavelet transform in the half-plane (b, a).

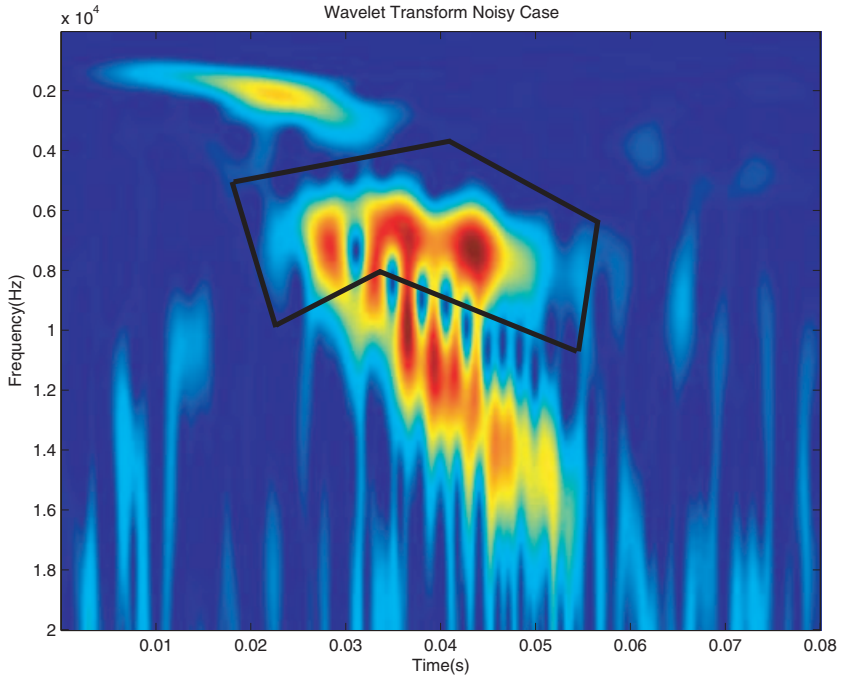

Figure 15. Modulus of the complex continuous wavelet transform (CCWT) of the input signal in presence of noise (signal/noise ratio equals 2). We note that even in the presence of a high level of noise, it is still possible to detect the different components present in the initial signal.

wave in the half-plane (b, a):

$$M_{fi}(b,a) = 0,\ E_{S_{fi}}(b,a) < \chi,$$
$$M_{fi}(b,a) = 1,\ E_{S_{fi}}(b,a) \geq \chi.$$

Let $\mathcal{D}_h$ be the domain defined by the polygon function h; the energy pattern related to a component $f_i(t)$ can be expressed as $E_{S_{fi}} = M_{fi}(b,a)E_{S_s}|_{\mathcal{D}_h}$. We have

$$E_{S_{fi}} = \iint |S_{fi}(b,a)|^2 \frac{dadb}{a^2} \leq c_g^{-1} \iint_{\mathcal{D}_h} |S_s(b,a)|^2 \frac{dadb}{a^2}, \quad (7)$$

where c_g is defined from the isometry property of the wavelet transform (Appendix eq. A4). $E_{S_{fi}}$ is therefore a function of finite energy.

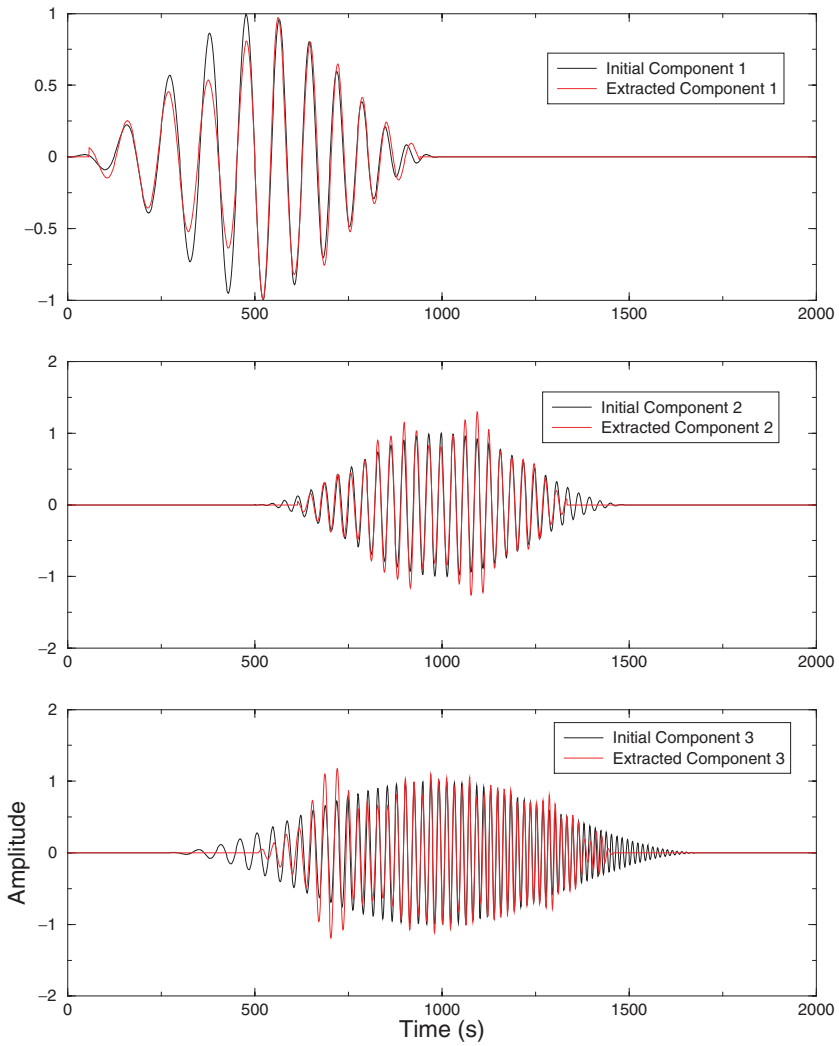

Figure 16. Presentation of the different components extracted using the algorithm developed in presence of noise. Each component is superimposed with the initial component to show the efficiency of the method.

$S_s(b, a)$ and $S_{fi}(b, a)$ verify the reproducing equation (eq. A9). We have

$$\iint_{\mathcal{D}_h} S_s(v,u)\mathcal{N}(v,u;b,a)\,\frac{dudv}{u^2} \tag{8}$$

$$= \iint S_{fi}(v,u)\mathcal{N}(v,u;b,a)\frac{dudv}{u^2}$$
$$= S_{fi}(b,a). \tag{9}$$

These previous equations clearly demonstrate that we can apply the inverse continuous transform (see Appendix).

The use of a progressive and modulated Gaussian function as an analysing wavelet (progressive Morlet-type wavelet) allows us to obtain an explicit formula of the reproducing kernel (Grossmann *et al.* 1989). Because this analysing wavelet is a function well localized in the time–frequency space, the associated kernel is well localized in the plane of the transform. We can remark that in the first approximation, the reproducing kernel $\mathcal{N}(b_o, a_o; b, a)$ can be considered as a Dirac function for the couples $\{a_o, b_o\}$.

This result is very important because it demonstrates that if we use a Morlet wavelet, the form of the mask is not important, it just helps to consider all the energy pattern of the signal we want to filter. If the mask includes some information far from the energy pattern of the signal, the contribution coming from this far information will not affect the results of the filtering. Therefore, it is possible to filter the component i of the signal $s(t)$ using the inverse continuous wavelet transform as

$$f_i(t) = \mathcal{R}e\left[c_g^{-1}\iint S_{fi}(b,a)g\left(\frac{t-b}{a}\right)\frac{dadb}{a^{3/2}}\right], \tag{10}$$

or to calculate directly from dilation parameter (Saracco & Tchamitchian 1990):

$$f_i(t_0) = \mathcal{R}e\left[k_g^{-1}\int S_{fi}(t_0,a)\frac{da}{a}\right], \tag{11}$$

where c_g and k_g are constants that depend only on the analysing wavelet g (see Appendix).

4.3 Application to synthetic data

Initially a synthetic signal composed by a sum of various wave trains was built (see Fig. 13). Fig. 14 presents its wavelet transform, which

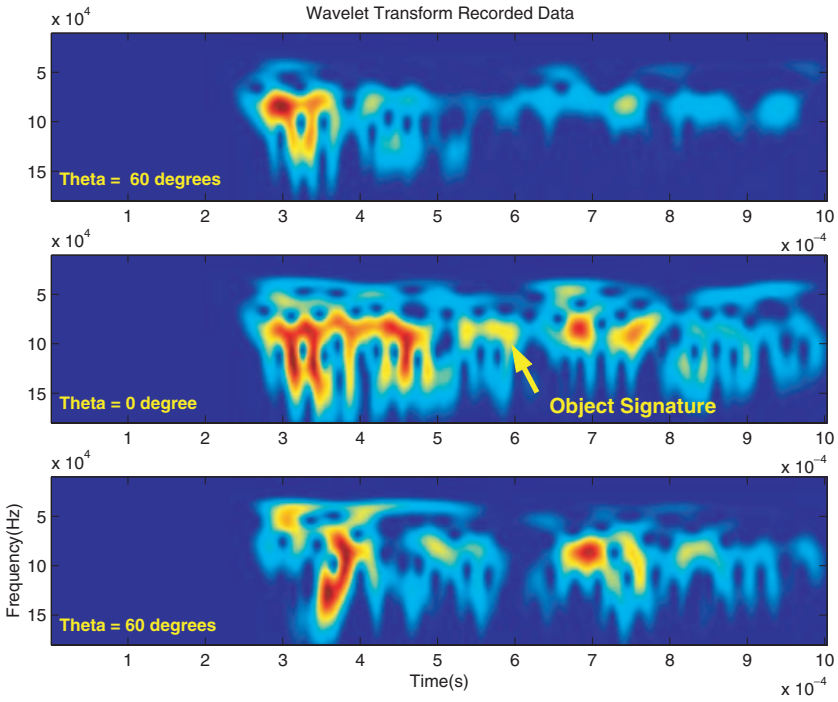

Figure 17. Time–frequency map computed for three traces recorded at the azimuth -60°, 0° and 60°. The presence of the target signature among a lot of borehole waves induces some difficulties to detect the target with standard techniques.

allows the discrimination between different components of the signal according to their characteristics (frequency, dispersion law of phase velocity, arrival time, etc.). Under asymptotic conditions of the signal with respect to the local properties of the analysing wavelet, it is possible to extract some ridges from the phase of the transform that characterize the frequency and amplitude modulation laws of the signal. The algorithms are based on the stationary phase approximation (Saracco *et al.* 1991). From ridges, the reconstruction of the signal (wave packet or echoes) is possible using the reproducing equation. The MSF process developed here has the advantage of characterizing and dissociating two close events (or waves) as you can see below with an additional ambient noise.

We select in the time–frequency domain the energy associated with each component that we want to filter. This is of importance because the algorithm will reconstruct only the part of the time–frequency selected by the mask, i.e. corresponding to the event we want to extract from the analysed signal. This operation is repeated for the different components of the signal. In a second step, a white Gaussian noise was added to the same set of data with a signal-to-noise ratio of 2. The continuous wavelet transform of this noisy data is shown Fig. 15. Fig. 16 presents the result of the different components extracted using the MSF and superimposed with the initial components of the original signal. We note that their reconstructions are in good accordance with respect to the true amplitude and frequency modulation laws of each wave train even with a high level of noise. It should also be noted that the reconstructions are performed without any assumption of the form of the mask. This processing is very effective in separating different components and in the recovery of their amplitudes with a good accuracy even in the presence of a high level of noise.

4.4 Application to acoustic data experiment

As previously explained, we want to extract information from the far field as a result of some discontinuities of the surrounding medium (materialized by the metallic plate). This event is hidden by the reflected waves of the ambient medium and by borehole waves. Their energy is then spread out in the time–azimuthal plane with a frequency range of 25–180 kHz.

Fig. 17 presents the wavelet transform map computed for three different traces recorded respectively at the azimuth position of -60°, 0° and 60°. The target is expected to be located around $\theta = 0^\circ$, between the times 0.55 and 0.6 ms, and with a frequency range around 70–120 kHz. The acoustic signature of the object can be clearly observed on the timescale plane for the azimuth zero and not on the two others maps. Looking at the data in three dimensions explains why the differentiation of the acoustic signature of the object is possible. A specific mask (polygon function) can be defined in the time–frequency domain and applied to each computed wavelet map corresponding to a trace in the time–azimuthal plane. Because the position of the target is invariant with respect to the azimuth, we applied the same polygon for all previously filtered traces with the help of the SMO method. Fig. 18 presents the result of the MSF and the reconstruction of the waves corresponding to the metallic plate.

The waves corresponding to the borehole waves have been successfully filtered thanks to the time–frequency filter. It is now possible to observe the echo corresponding to the target among a weak ambient noise. It still remains around the same azimuth, some arrivals with low energy corresponding to the multiple reflections on the target. These waves arrive at the same time and present the same frequency range as that of the signal of interest. It shows the difficulty of filtering data in such environment. Fig. 19 presents the spectral density of the filtered data in the frequency–azimuthal plane. We see clearly that the maximum of the energy is located in the neighbourhood of the object and decays very fast with a ratio of 3. Fig. 20 presents the final result after the energy in the time–azimuthal plane has been refocused thanks to the AMO correction (Valero *et al.* 2001). The first arrival time ($t \simeq 0.54$ ms) of the wave train

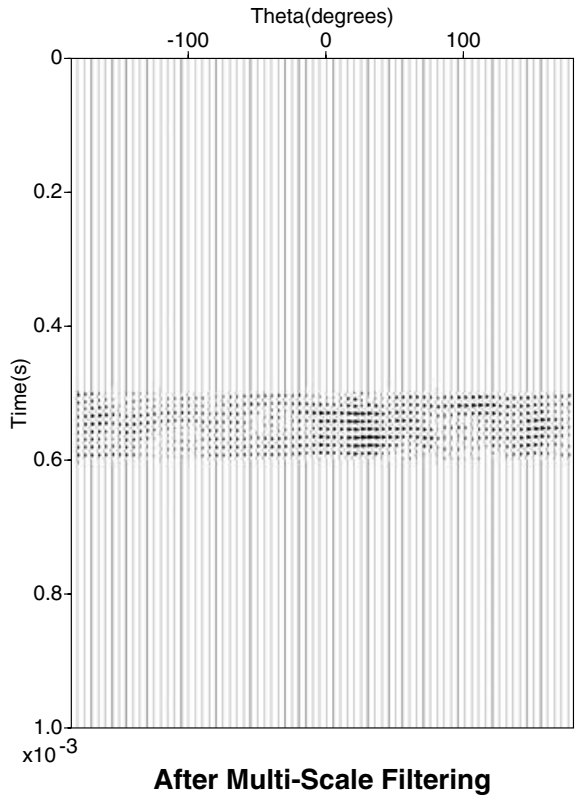

Figure 18. Result after the multiscale filtering (MSF). The strong borehole waves and the refracted signal resulting from the junction of the pipe are removed. Some waves are still present on the other traces but they are of weak amplitude compared with the target echo.

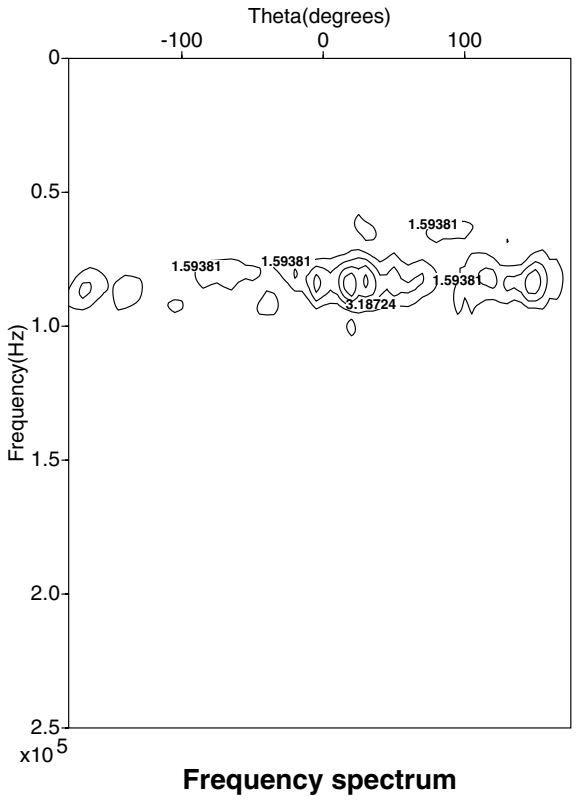

Figure 19. Frequency spectrum of the data in the azimuthal–frequency plane after wavelet filtering. The main energy is located around 0° where the target is expected, with an energy ratio of 3. This result allows us to demonstrate that the other detected signals are some residuals as a result of weak multiple reflections of the target and the ambient noise.

corresponds to the wave front of the metallic plate and a weak noise corresponding to the multiple reflection on the wall tank around -180° and 180°.

5 COMPARISON WITH COVARIANCE METHOD

We want to compare the SMO and MSF filtering to well-known covariance methods often used in seismic signal processing and geophysical prospection (Hsu 1990; Kirlin & Done 1999). We recall briefly the principle of this method. Let us consider experimental data as a matrix X of M traces of N samples, such that $M \geq N$. The SVD methods are based on this following property: $\mathsf{X} = \mathsf{U}\mathsf{D}\mathsf{V}^T$, where U and V are respectively $M \times N$ and $N \times N$ orthogonal matrices, V^T is the transpose matrix of V, and D is a diagonal $N \times N$ matrix with positive or zero elements, the singular values. We can write

$$\mathbf{X} = \sum_{i=1}^{N} \sigma_i \mathbf{u}_{ik} \mathbf{v}_{ki}, \tag{12}$$

where $\mathbf{u}_{i\mathrm{k}}$ and $\mathbf{v}_{k\mathrm{i}}$ are the ith eigenvector of $\mathsf{X}\mathsf{X}^T$ and $\mathsf{X}^T\mathsf{X}$ respectively, and σ_i is the ith singular value of X. σ_i is the positive square root of the eigenvalues of the matrices $\mathsf{X}\mathsf{X}^T$ and $\mathsf{X}^T\mathsf{X}$. These eigenvalues are always positive as a result of the positive definite nature of matrices.

If most of the singular values are very small, X will be well approximated (reconstructed), only by a few eigenvalues. The previous equation shows clearly that the reconstruction of the matrix X can be seen as the sum of different images, weighted by the corresponding eigenvalues. In this case, we consider an image as a seismic section of dimension $(\mathbf{u}_{i\mathrm{k}}\mathbf{v}_{k\mathrm{i}}^T)$. The principle of the filtering is just to consider how a seismic section can be decomposed into a sum of different reflectors related to the signal and a residual section of noise. We define the noise as the part of the information that is of no interest. Freire & Ulrych (1988), defined three eigenimages as three filters: the bandpass X_{BP}, the low-pass X_{LP} and a high-pass X_{HP} in terms of ranges of the singular values used in the reconstruction of the matrix X. The bandpass image is reconstructed by rejecting the uncorrelated and correlated traces and it is given by

$$\mathbf{X} = \sum_{i=p}^{q} \sigma_i \mathbf{u}_{ik} \mathbf{v}_{ki}^T, \quad 1 < p \leq q < N. \tag{13}$$

The summation of the X_{LP} is defined from $i = 1$ to $p - 1$ and X_{HP} from $i = q + 1$ to N (Hemon & Mace 1978). The choice of p and q depends on the relative magnitudes of the singular values, which are functions of the observed data. In practice, these parameters are estimated from a plot of the eigenvalues as a function of the index i.

We applied the same kind of techniques in order to detect the acoustic signature of the target. The plot of the eigenvalues computed from the raw data (*cf.* Fig. 4) is presented in Fig. 21. We observe that the highest eigenvalues are the first three ones. As expected, the image is reconstructed (Fig. 22) with the most energetic arrival related to the highest eigenvalues. The acoustic signature of the object is not observed because it is at the level of the noise. To avoid this problem, we subtract the reconstructed section from the initial ones. Results are presented Fig. 23. As expected, the strong borehole

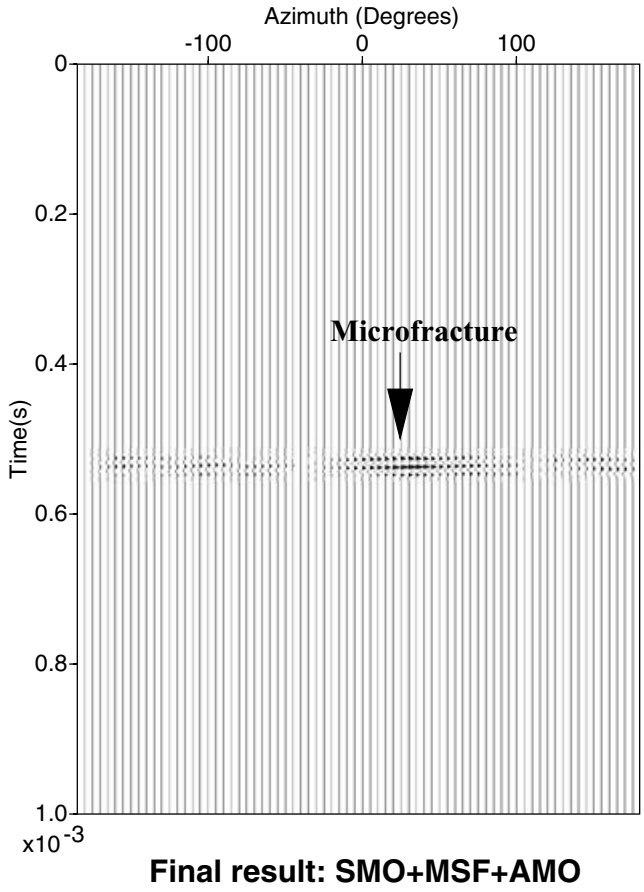

Figure 20. Final result obtained after Stoneley move out (SMO) and azimuthal move out (AMO) correction combined with the multiscale filtering (MSF). All borehole waves have been removed and it becomes easy to detect the position of the fracture in the azimuth–time domain.

waves are removed but other undesired wave fronts remain that hide the arrival of interest. The result is similar when we increase the number of eigenvalues (Fig. 24). The SVD method partially filters borehole waves, but does not allow us to localize the target in the azimuthal–time domain, because of the low signal-to-noise ratio. An alternative that could improve results is to first apply an SMO filtering (see Fig. 25). In this case, the obtained results are comparable to Fig. 12 before applying the MSF. In comparison, the methods we proposed are not so sensitive to the signal-to-noise ratio and they give good results when the common techniques failed.

6 CONCLUSION

We presented in this study two algorithms to filter borehole waves and extract information about the formation surrounding the borehole (fracture, cavity, etc. . .). The algorithms are used in conjunction with seismic endoscopy applications. Experimental tests in an acoustic tank illustrated the potentiality of the proposed methods. The first one, called SMO, performs a dynamic correction of borehole waves. This method is based on the fact that a borehole wave will be seen as a plane reflector (or straight line) in the azimuthal–time domain (invariance symmetry of tube waves, or borehole waves). This property has been exploited to remove borehole waves from the recorded section. The second one, based on the wavelet theory, allows us to perform an MSF and the reconstruction of some details of the far field. The idea is to extract, from the total reflected waves, some weak information coming from the surrounding medium, with the help of the properties of the kernel reproducing and of the analysing wavelet itself. Both algorithms were applied to real and synthetic noisy data. Moreover, the azimuthal information provided by the probe offers a new investigation tool for looking at borehole data, in particular to discriminate in the (θ, t) plane reflected borehole waves from the reflected waves of weak energy coming from the far field. Comparisons with the SVD method points out the efficiency of coupling SMO and MSF, when there is

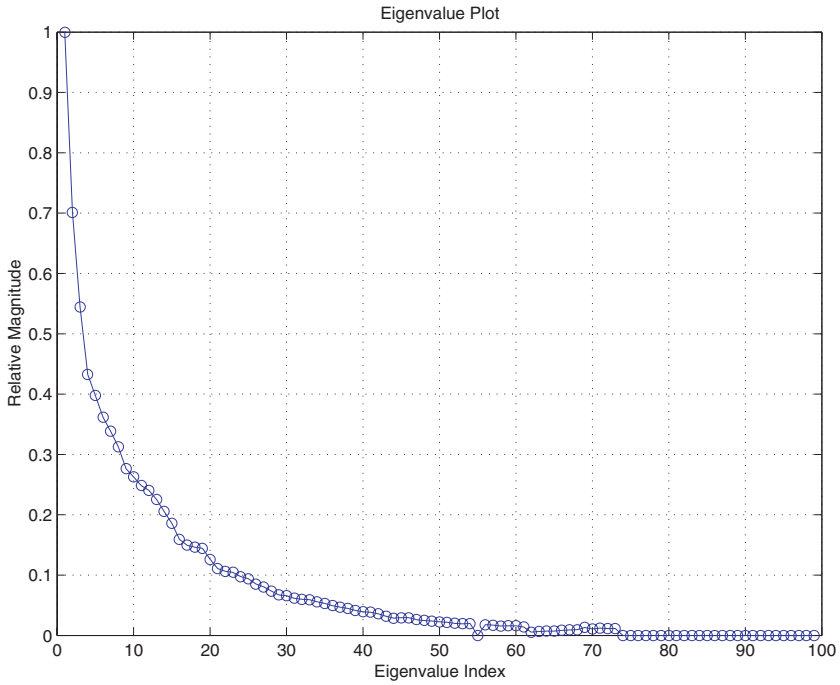

Figure 21. Relative magnitude of the eigenvalues computed for the raw data.

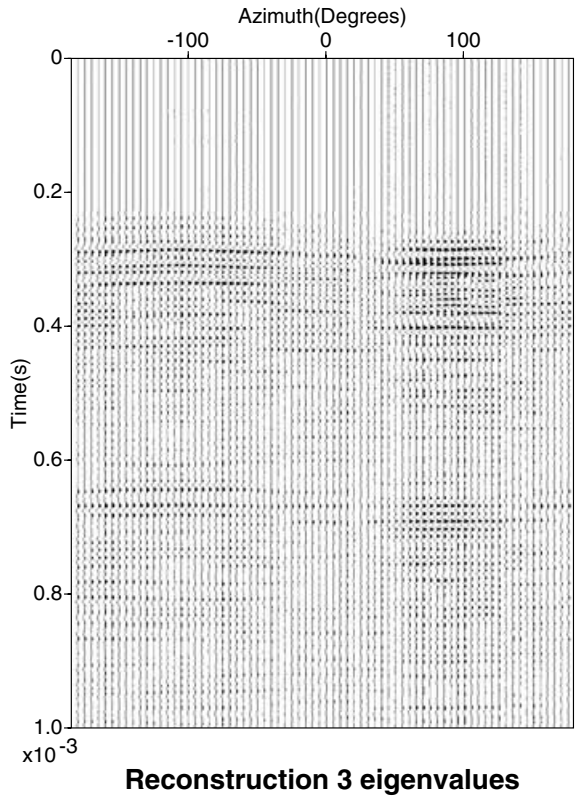

Figure 22. Reconstructed waveform using only three eigenvalues. It is not possible to observe an echo corresponding to the object.

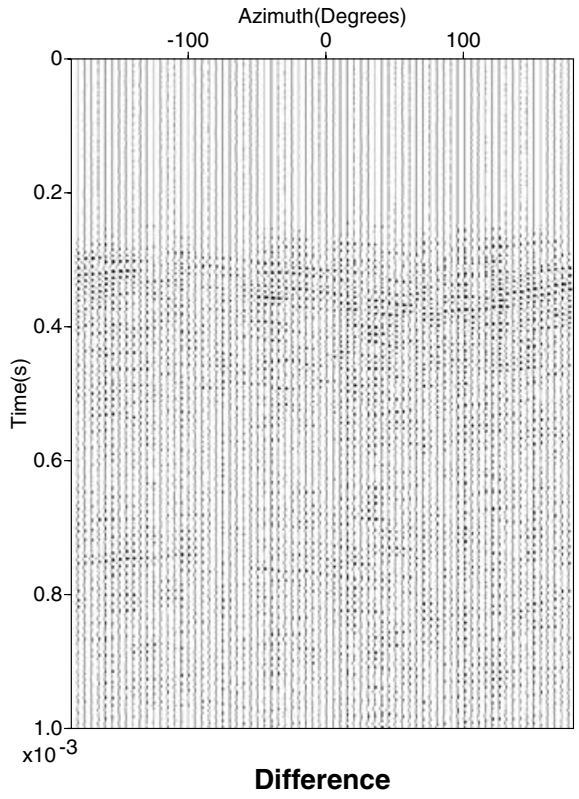

Figure 23. Difference between the raw data and the reconstructed section with three eigenvalues. The amplitude of strong borehole waves decreases but some of them still remain. It is not possible to detect the acoustic signature of the metallic plate.

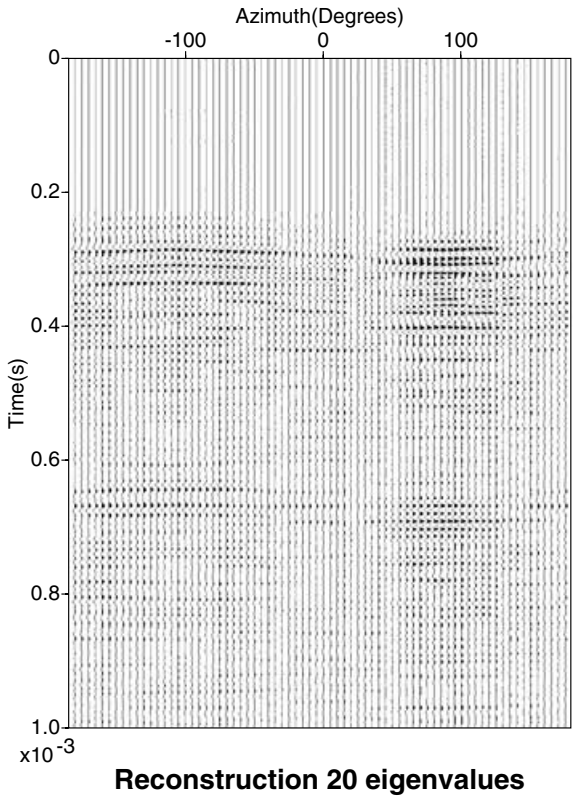

Figure 24. Reconstructed waveform using 20 eigenvalues.

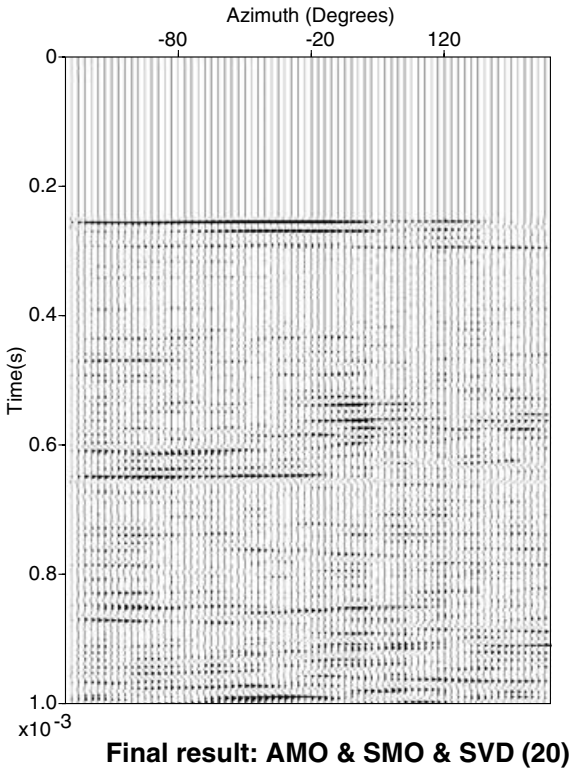

Figure 25. Final result: reconstructed waveform using 20 eigenvalues after azimuthal move out (AMO) and Stoneley move out (SMO) correction. Only a multiscale filtering (MSF) allows to filter borehole waves and to reconstruct, with accuracy, some details of the far field.

a low signal-to-noise ratio. Results on synthetic and real acoustic data were in good agreement.

ACKNOWLEDGMENTS

We want to thank particularly M. LeMoine (Géosciences-Rennes) for his help and collaboration in the development of the probe, A. Grossmann for his fruitful discussions and advice, and the referees, in particular G. Lambaré, for their constructive remarks and suggestions. One of the authors (HPV) would like to thank D. Gibert (Géosciences-Rennes) for his strong support during the development of the project. This work, initially supported by the Centre National de la recherche scientifique (CNRS)-Institut National des Sciences de l'univers (INSU) Géomécanique des Roches Profondes (GdR), is financially supported by the CNRS and Agence nationale pour la gestion des déchets radioactifs (ANDRA) through the GdR FORPRO (research action number 99-II) and corresponds to the GDR FORAGE PROFOND contribution number 2002/20 A. We thank Yves Guéguen, Joël Lancelot and Patrick Lebon for their strong support since the beginning of this project.

REFERENCES

Avis, J.L. & Annan, A.P., 1989. Ground penetrating radar for high-resolution mapping of soil and rock stratigraphy, *Geophys. Prospect.,* **37,** 531–551.

Bendat, S. & Piersol, A.G., 1986. *Random Data: Analysis and Measurement Procedures,* Wiley-Interscience, New York.

Burger, H.R., 1992. *Exploration geophysics of the shallow subsurface,* Prentice-Hall, Englewood Cliffs, NJ.

Cheng, C.H. & Toksoz, N.M., 1981. Elastic wave propagation in a fluid-filled borehole and synthetic acoustic logs, *Geophysics,* **46**(7), 1042–1053.

Cheng, C.H., Toksoz, N.M. & Willis, M.E., 1982. Determination of in situ attenuation from full waveform acoustic logs, *J. geophys. Res.,* **87**(B7), 5477–5484.

Cohen, J.K. & Stockwell, J.W., Jr, 2001. *CWP/SU: Seismic Unix Release 35,* Center for Wave Phenomena, Colorado School of Mines, Golden, CO.

Dobrin, M.B., 1983. *Introduction to geophysical prospecting,* 3rd edn, McGraw-Hill, New York.

Fisher, E., 1992. Acquisition and processing of wide-aperture ground penetrating radar data, *Geophysics,* **57**(3), 495–504.

Freire, S.L.M. & Ulrych, T.J., 1988. Application of singular value decomposition to vertical seismic profile, *Geophysics,* **53,** 778–785.

Gradshteyn, I.S. & Ryzhik, I.M., 1990. *Table of Integrals, Series and Products,* Academic-Press, New York.

Grossmann, A. & Morlet, J., 1984. Decomposition of Hardy functions into square integrable wavelets of constant shape, *SIAM J. Math. Anal.,* **15,** 723–736.

Grossmann, A., Kronland-Martinet, R. & Morlet, J., 1989. Reading and understanding continuous wavelet transform, in *Wavelet, Time–frequency Methods and Phase Space,* pp. 2–20, eds Combes, J.M., Grossmann, A. & Tchamitchian, P., Springer-verlag, Berlin.

Hardage, B.A., 1983. *Vertical Seismic Profiling, A: profiling, Geophysical exploration,* Geophysical Press, Amsterdam.

Hardin, E.L., Cheng, C.H., Paillet, F.L. & Mendelson, J.D., 1987. Fracture charecterization by means of attenuation and generation of tube waves in fractured crystalline rock at mirror lake, New Hampshire, *J. geophys. Res.,* **92**(B8), 7989–8006.

Hemon, C.H. & Mace, D., 1978. Essai d'une application de la transformee de Karhunen-Loeve au traitement sismique, *Geophys. Prospect.,* **26,** 600–626.

Hornby, B.E., 1989. Imaging of near-borehole structure using full-waveform sonic data, *Geophysics,* **54**(6), 747–757.

Hsu, K., 1990. Wave separation and feature extraction of acoustic well-logging waveforms using Karhunen-Loeve transformation, *Geophysics,* **55**(2), 176–184.

Kelly, W.E. & Mares, S., 1993. *Applied Geophysics in Hydrogeological and Engineering Practice,* 44, Elsevier Science, London.

Kimball, C.V. & Marzetta, T.L., 1987. Semblance processing of borehole acoustic data, *Geophysics,* **49,** 530–544.

Kirlin, R.L. & Done, W.J., 1999. Covariance analysis for seismic signal processing, Vol. 8, Soc. Expl. Geophys., Tulsa, OK.

Morlet, J., Arens, G., Fourgeau, I. & Giard, D., 1983. Wave propagation and sampling theory, *Geophysics,* **47,** 203–236.

Nobes, D.C., 1996. Troubled waters: Environmental applications of electrical and electromagnetic methods, *Surv. Geophys.,* **17,** 393–454.

Oristaglio, M., 1985. A guide to current uses of vertical seismic profiles, *Geophysics,* **50,** 2473–2479.

Paillet, F.L. & Cheng, C.H., 1991. *Acoustic waves in borehole,* CRC, Boca Raton, FL.

Paillet, F.L. & White, J.E., 1984. Acoustic modes of propagation in the borehole and their relationship to rock properties, *Geophysics,* **47**(8), 1215–1228.

Papoulis, A., 1984. *Random Variables and Stochastic Processes,* McGraw-Hill, New York.

Saracco, G., 1989. Acoustic propagation through an inhomogeneous medium in harmonic and transient regime: Asymptotic methods and Wavelet transforms, *PhD thesis,* CNRS-UPR 7051-LMA & UER II, Campus de Luminy, Marseille, France.

Saracco, G., 1994. Propagation of transient waves through a stratified fluid medium: Wavelet analysis of a nonasymptotic decomposition of the propagator, *J. acoust. Soc. Am.,* **95**(3), 1191–1205.

Saracco, G. & Tchamitchian, Ph., 1990. Retrieval of a time-dependent source in an acoustic propagation problem, in *Inverse Problems in Action (Inverse Problems and Theoretical Imaging),* pp. 207–211, ed. Sabatier, P.C., Springer-Verlag, Berlin.

Saracco, G., Sessarego, J., Sageloli J., Guillemain, P. & Kronland-Martinet, R., 1991. Extraction of modulation laws of elastic shells by the use of wavelet transform, in *Research notes in Applied Mathematics: Wavelets and Applications,* pp. 61–68, eds Meyer, Y. & Paul, T., Masson-Springer, Paris.

Tubman, K.M., Cheng, C.H. & Toksoz, N.M., 1984. Synthetic full waveform acoustic logs in cased boreholes, *Geophysics,* **49**(7), 1052–1059.

Valero, H.P., 1997. Mise au point d'une méthode d'endoscopie sismique 3D en géophysique de puits: Développements & Traitement de l'information, *PhD thesis,* IPG, Paris, and Geosciences, Rennes, France.

Valero, H.P., Saracco, G. & Gibert, D., 2001. Three-Dimensional Seismic endoscopy-Part I: Design of apparatus and basic Imaging Algorithms, *IEEE T. Geosci. Remote,* **39**(10), 2262–2274.

Valero, H.P., Gautier, S., Saracco, G. & Holschneider, M., 2002. Deconvolution from instrumental devices and source effect in acoustic experiemnts, *IEEE T. Instrum. Meas.,* **51**(2), 268–276.

Winkler, K.W., Liu, H.L. & Johnson, D.L., 1989. Permeability and boreholes stoneley waves: Comparison between experiment and theory, *Geophysics,* **54**(1), 66–75.

Zemanek, J., Glenn, E.E., Norton, L.J. & Caldwell, R.L., 1970. Formation evaluation by inspection with the borehole televiewer, *Geophysics,* **35**(2), 254–269.

APPENDIX A: RECALL: CCWT AND REPRODUCING KERNEL

Let $s(p)$ be an arbitrary time or space dependence signal, and $g(p)$ the chosen complex and progressive analysing wavelet, necessary to study wave propagation phenomena (Saracco 1989). a and b represent respectively the dilation and the translation parameter. The continuous wavelet transform $S(b, a)$ of a function $s(p)$ is the scalar product of this signal by the dilated (contracted) and translated wavelets family g, such as $T^b D^a[g(p)] = a^{-1/2} g(\frac{p-b}{a})$. It follows:

$$S(b,a) = \langle T^b D^a[g(p)], s(p)\rangle = a^{-1/2} \int s(p)\overline{g}\left(\frac{t-b}{a}\right)dp, \quad \text{(A1)}$$

where $\overline{g}$ is the complex conjugate of g. g is chosen to be analytic or progressive [i.e. $\hat{g}(\omega) = 0$, for negative (spatial or time) frequency components $\omega < 0$].

Let p be the time variable. The translation parameter b is then homogeneous to the time, while the scale parameter can be interpreted like a zoom. This number defined to be strictly positive. Small dilations will be related to the high frequencies and reverse. The choice of the analysing wavelet is free but its has to verify the admissibility condition deduced from the isometric property of the transform in the following sense: there exists for every $s(t)$ a constant c_g depending only on the wavelet g such that:

$$\int |s(t)|^2 dt = c_g^{-1} \iint |S(b, a)|^2 \frac{dadb}{a^2} \tag{A2}$$

and

$$c_g = 2\pi \int \frac{|\hat{g}(\omega)|^2}{|\omega|} d\omega. \tag{A3}$$

$\hat{g}$ is the Fourier transform of g and ω is the dual variable of the time t. It follows that g is of zero mean [$\int g(t)dt = 0$ or $\hat{g}(0) = 0$]. If this condition is satisfied, there exists an inversion formula, which reconstructs the analysed signal (Saracco 1989):

$$s(t) = Re\left[c_g^{-1} \iint S(b, a) a^{1/2} \overline{g}\left(\frac{t-b}{a}\right) \frac{dadb}{a^2}\right], \tag{A4}$$

where $Re[.]$ represents the real part.

It can be shown also that $s(t)$ verifies a simple inversion formula (Saracco & Tchamitchian 1990) involving only a one-dimensional (1-D) integral over the dilation parameter:

$$s(t) = Re\left[k_g^{-1} \int S(t, a) \frac{da}{a^{3/2}}\right]. \tag{A5}$$

The analysing wavelet verifies the following admissibility condition:

$$\int \frac{|\hat{g}(\omega)|}{|\omega|} d\omega < \infty \quad \text{and} \quad k_g = 2\pi \int \frac{|\hat{g}(\omega)|}{|\omega|} d\omega.$$

Because the continuous wavelet transform (CWT) is non-orthogonal, $\langle g(b, a), g(b', a')\rangle \neq 0$. There exists a reproducing kernel $\mathcal{N}_g$ defined from eqs (A1) and (A3) as

$$\mathcal{N}_g(b, a, v, u) = C_g^{-1} \langle g(b, a), g(v, u)\rangle. \tag{A6}$$

Let $\mathcal{N}_g(v, u; 0, 1) = C_g^{-1} \langle T^u D^v g, \overline{g}\rangle$.

$\mathcal{N}_g$ verifies the following:

$$\mathcal{N}_g(v, u; b, a) = \mathcal{N}_g\left(0, 1; \frac{v-b}{u}, \frac{a}{u}\right).$$

$\mathcal{N}_g$ is then a function of scale ratio $\frac{a}{u}$ with a distance defined in scale ratio $\frac{v-b}{u}$. It reflects the coherence of the wavelet coefficient in the half-plane (b, a) (timescale resolution of the wavelet). Its modulus $|\mathcal{N}_g|$ has a maximal value when the couples $\{b, a\} = \{v, u\}$ and decays quickly when the distance from the couple $\{v, u\}$ increases, it means $\frac{a}{u} \approx 1$, $\frac{v-b}{u} \gg 1$.

We choose a progressive analysing wavelet of Morlet type such that $g(t) = \exp(i\omega_0 t) \exp(\frac{-t^2}{2\beta^2})$, here, $\omega_0 = 2\pi$, $\beta = 1$ with $\hat{g}(\omega) = 0$ for $\omega < 0$ (Saracco 1994). Let us denote $a' = \frac{a}{u}$ and $b' = \frac{v-b}{u}$, using (Gradshteyn & Ryzhik 1990) the modulus and the phase of the Kernel reproducing has the explicit form:

$$|\mathcal{N}_g(0, 1; b', a')| = \frac{\beta a'}{C_g} \sqrt{\frac{2\pi}{1 + a'^2}} \times \exp\left[-\frac{1}{2} \frac{\omega_0 \beta^2 (a' - 1)^2 + b'^2}{1 + a'^2}\right]; \tag{A7}$$

$$\arg[\mathcal{N}_g(0, 1; b', a')] = \frac{\omega_0 b'(1 + a')}{1 + a'^2}.$$

It follows:

$$|\mathcal{N}_g(v, u; b, a)| = \frac{\beta a}{c_g} \sqrt{\frac{2\pi}{u^2 + a^2}} \times \exp\left[-\frac{1}{2} \frac{\omega_0 \beta^2 (a^2 - u^2) + (v - b)^2}{a^2 + u^2}\right]; \tag{A8}$$

$$\arg[\mathcal{N}_g(v, u; b, a)] = \frac{\omega_0 (v - b)(u + a)}{u^2 + a^2}.$$

From eqs (A1) and (A3), all wavelet coefficients verify the reproducing equation:

$$S(v, u) = \int S(b, a) \mathcal{N}_g(v, u, b, a) \frac{dbda}{a^2}. \tag{A9}$$

It allows, by using the interpolation formula introduced by Grossmann *et al.* (1989), to reconstruct an approached value of the CWT from the value of the discrete wavelet transform (DWT). Some details of the surrounding medium will be reconstructed with the help of the reproducing equation (Section 4).